

Evolution of Colloidal Nanocrystals: Theory and Modeling of their Nucleation and Growth

Joel van Embden,[†] John E. Sader,[‡] Malcolm Davidson,[§] and Paul Mulvaney^{*,†}

School of Chemistry and Bio21 Institute, University of Melbourne, Parkville, Victoria, 3010, Australia,
Department of Mathematics and Statistics, University of Melbourne, Parkville, Victoria, 3010, Australia, and
Department of Chemical and Biomolecular Engineering, University of Melbourne, Parkville,
Victoria, 3010, Australia

Received: March 27, 2009; Revised Manuscript Received: July 3, 2009

Through the use of a population balance equation (PBE), the nucleation and growth of nanocrystals evolving under various initial reaction conditions are simulated. Simulations of nanocrystal (NC) growth in both the diffusion and reaction limits are presented, and it is concluded that NC growth proceeds under strongly reaction-limited kinetics. The particle size distributions obtained in the asymptotic diffusion and reaction limits were found to be slightly narrower than the stationary distributions predicted by LSW and Wagner theories, respectively. There is strong experimental evidence indicating that the early stages of NC synthesis involve simultaneous nucleation, growth and coarsening. The simulations performed here are able to replicate these conditions, providing insight into the factors that govern these early time processes, as well as the consequences they have at longer reaction times.

Introduction

Experimental investigations designed to reveal the underlying mechanisms of colloid nucleation and growth have spanned many decades.^{1–8} Scientific curiosity, as well as the increasing number of technologies that use colloid particles, continues to fuel this interest. Complementary to these experimental investigations, mathematical investigations on colloid formation have also been conducted.^{9–11} In addition, numerical models describing the nucleation and growth of near-micrometer-sized colloids¹² and binary alloys,^{13–15} as well as Ostwald ripening,^{16,17} have been reported. Other studies have focused solely on the numerical issues involved in effectively modeling mass transport.^{18–21}

Despite the plethora of literature on the numerical modeling of colloid formation, to date there exist few reports that contain simulations of nanoparticle nucleation and growth,^{22–27} presumably due to the fact that reliable experimental data on such systems have emerged only recently. Although valuable information can be gleaned from such reports, most of the current models on nanoparticle evolution suffer from a failure to accurately simulate nucleation and growth under experimentally realistic conditions. A common misinterpretation is that NC growth proceeds under diffusion limited conditions.^{1,23} Further inaccuracies have arisen from the use of inappropriate values for the monomer diffusion coefficients²⁸ or unrealistic monomer concentrations.²²

In this article we focus on simulating the nucleation and growth of nanocrystals from a homogeneous solution of monomer in the liquid phase. Throughout this work the term “monomer” will be taken to be the single atomic unit used for both nucleation and growth. It should be noted that the active monomer unit is that which is liberated from the breakdown of the precursor molecule. This article has been

divided into three main sections. In the first section we derive the rate expressions necessary to describe nanoparticle nucleation and growth. To begin we focus on single-particle growth dynamics. Using steady-state assumptions we derive a flexible expression for the single-particle growth rate that is tunable between the diffusion and reaction limits. Next, derivation of the nucleation rate is presented. To ensure mass balance, a governing equation that keeps track of the movement of monomer is then outlined. In the second section the details of the numerical scheme employed to solve the relevant rate equations is presented along with test simulations that highlight the stability and accuracy of the scheme. In the final section simulations on NC growth only and simultaneous nucleation and growth are presented. We conclude by presenting simulations designed to model the nucleation and growth of CdSe nanocrystals prepared by the common “hot injection” method.

In order to gain the greatest insight into the mechanisms that govern nanocrystal nucleation and growth, care was taken to ensure the simulation conditions were as close to realistic experimental conditions as possible. It should be noted that although the simulations performed here have focused on the formation of nanocrystals in the liquid phase via the “hot injection” method, the governing equations and numerical scheme may be directly applied to the formation of micrometer-sized particles, as well as to different reaction strategies.

Theoretical Model

Single-Particle Growth Dynamics. To derive the relevant rate equations for particle growth, consider Figure 1. For an isolated particle dispersed in a homogeneous solution of monomer with a concentration $[C]_b$, growth takes place in two distinct steps. Monomers are brought to the particle surface via diffusion from the bulk solution at a rate determined by the diffusion coefficient D . These monomers may then react with the particle (become incorporated into the lattice) with a rate determined by k_r . In addition, monomers may desorb from the particle (particle dissolution) at a rate determined by k_{des} .

* To whom correspondence should be addressed. E-mail: mulvaney@unimelb.edu.au.

[†] School of Chemistry and Bio21 Institute.

[‡] Department of Mathematics and Statistics.

[§] Department of Chemical and Biomolecular Engineering.

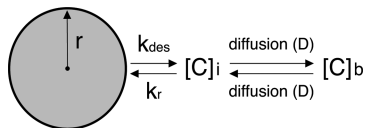


Figure 1. Schematic showing an isolated particle of radius r . $[C]_b$ and $[C]_i$ are the bulk and interfacial monomer concentrations, respectively. Monomer is transported to and from the particle/solution interface by diffusion at a rate determined by the diffusion coefficient D . The incorporation of monomer into the particle (particle growth) is controlled by the rate constant k_r . Likewise the removal of monomer from the particle (particle dissolution) is controlled through the rate constant k_{des} .

As stated by Fick's first law the total flux (I) of molecules through a (diffusion) sphere of radius σ is given by

$$I_{diff} = 4\pi\sigma^2 J = 4\pi\sigma^2 D \left. \frac{d[C]}{d\sigma} \right|_{\sigma \geq r} \quad (1)$$

where D is the diffusion coefficient of the monomer. The boundary conditions for the integration of eq 1 are that at $\sigma = \infty$ the concentration of monomer is equal to the value in the bulk solution ($[C] = [C]_b$) and that at $\sigma = r$ the concentration of monomer is equal to the interfacial concentration ($[C] = [C]_i$). Also, under steady-state conditions I_{diff} is a constant independent of σ . After performing the integration we obtain the total diffusive flux of monomer to the surface of the particle:

$$I_{diff} = 4\pi r D ([C]_b - [C]_i) \quad (2)$$

For a first-order surface reaction, the total flux of monomer at the surface of a spherical particle depends on the interfacial concentration $[C]_i$, as well as the reaction (k_r) and desorption (k_{des}) rate constants as

$$I_{react} = k_{obs} [C]_b = 4\pi r^2 (k_r [C]_i - k_{des}) \quad (3)$$

where k_{obs} is the observed rate constant. In the steady state, the diffusive and reactive fluxes of monomer at the surface are equal ($I_{diff} = I_{react}$). Thus, combining eqs 2 and 3 and then solving for the interfacial concentration we obtain

$$[C]_i = \frac{D[C]_b + k_{des}r}{k_r + D} \quad (4)$$

The limiting condition is that monomer may not react at a rate faster than it may diffuse to the surface. Equation 4 gives the monomer concentration at $\sigma = r$. Substituting eq 4 into Fick's Law, eq 2, then gives the total flux of monomer:

$$I^{ss} = 4\pi r D \left[[C]_b - \left(\frac{D[C]_b + k_{des}r}{k_r + D} \right) \right] \quad (5)$$

where we have introduced the condition for equilibrium solubility with respect to a particle of radius r as $[C]_e = k_{des}/k_r$. Given that the total steady-state flux, I^{ss} , scales with volume over time, it can be expressed through the growth rate as

$$I^{ss} = \frac{d}{dt} \frac{4\pi r^3}{3V_m} = \frac{4\pi r^2}{V_m} \frac{dr}{dt} \quad (6)$$

where V_m is the molar volume of the monomer. Furthermore, the equilibrium concentration, $[C]_e$, is given by the Gibbs–Thomson equation:

$$[C]_e = [C]_{\infty} \exp \left\{ \frac{2\gamma V_m}{rRT} \right\} \quad (7)$$

where $[C]_{\infty}$ is the concentration of monomer in equilibrium with an infinitely flat surface. (Derivation of the growth rates in both the pure diffusion and pure reaction limits may be accomplished as follows. In the pure diffusion limit monomer reacts instantly at the surface, hence $[C]_i \approx [C]_e$. In the pure reaction limit, monomer diffuses to the particle surface but reacts at a rate dependent upon the nature and concentration of adsorbates in solution, hence $[C]_i \approx [C]_b$. Combining eqs 2 and 6 or eqs 3 and 6, noting that $[C]_e = k_{des}/k_r$, with the first two terms in the Taylor expansion of eq 7 leads to expressions for the growth rate in the pure diffusion or pure reaction limits, respectively. The form of these equations was first outlined by Sugimoto et al.¹²) To effectively model nanoparticle growth it is useful to establish a form of the growth rate that is able to be tuned between the reaction and diffusion limits. Substituting eqs 5 and 7 into eq 6 gives the instantaneous size-dependent growth rate:

$$\Gamma_r = \frac{dr}{dt} = \frac{DV_m \left([C]_b - [C]_{\infty} \exp \left\{ \frac{2\gamma V_m}{rRT} \right\} \right)}{\left(r + \frac{D}{k_r} \right)} \quad (8)$$

The form of the growth rate is similar to that obtained by other authors.^{13,22,25} To calculate the growth rate it is convenient to convert eq 8 into dimensionless units. The growth rate then becomes

$$\frac{d\beta}{d\tau} = \frac{\left(S - \exp \left\{ \frac{1}{\beta} \right\} \right)}{(\beta + \xi)} \quad (9)$$

where we have introduced the following dimensionless radius, supersaturation and time:

$$\beta = r\phi \quad \text{Dimensionless radius} \quad (10)$$

$$S = \frac{[C]_b}{[C]_{\infty}} \quad \text{Supersaturation} \quad (11)$$

$$\tau = t\psi \quad \text{Dimensionless time} \quad (12)$$

with

$$\phi = \frac{RT}{2\gamma V_m}, \quad \psi = \phi^2 DV_m [C]_{\infty} \quad (13)$$

The ratio of diffusion to reaction rates is given by the dimensionless Damköhler number:

$$\xi = \frac{D\phi}{k_r} \quad (14)$$

We note here that as the Damköhler number is increased the growth rate asymptotes to zero. If $k_r \ll D$ then $\xi \gg 1$ and the kinetics of growth are *reaction limited*: The relatively low rate of reaction at the surface limits the incorporation of monomer into the particle. Conversely, if $\xi \ll 1$ then the process is *diffusion limited*: The reaction rate is determined by the rate at which monomers diffuse to the nuclei. For plots of the growth rate as a function of various reaction parameters see the Supporting Information.

Nucleation. The above section is concerned with the rate of growth of an existing particle. In this section a source term is developed, which accounts for the formation of particles. The source term has been derived within the framework of Equilibrium Theory. First let us consider the simple case for the reaction of a monomer unit, C , with a cluster of n units:



The above reaction has the equilibrium constant:

$$K_{1,n} = k_{1,n}/k_{-1,n} = \frac{[C_{n+1}]}{[C][C_n]} \quad (16)$$

The Gibbs free energy change under standard state conditions for $C + C_n \rightarrow C_{n+1}$ is given by $\Delta G_{1,n}^0 = -k_B T \ln K_{1,n}$ and for the condensation reaction of monomer onto an infinitely large particle, C_∞ , by $\Delta G_{1,\infty}^0 = -k_B T \ln K_{1,\infty}$. The difference in the Gibbs energy between (1) adding a monomer unit to an infinitely large particle and (2) that of a particle with a finite number of units, n , then gives the sum of the surface and volume free energy changes for the particle upon addition of the monomer unit. That is, $\Delta G_{1,n}^0 - \Delta G_{1,\infty}^0 = \Delta G_{1,n}^{\text{vol}} + \Delta G_{1,n}^{\text{surf}}$. Combining these expressions, we obtain

$$-k_B T \ln(K_{1,n}/K_{1,\infty}) = \Delta G_{1,n}^{\text{vol}} + \Delta G_{1,n}^{\text{surf}} \quad (17)$$

$K_{1,\infty}$ is the reciprocal of the monomer concentration in equilibrium with a flat surface, $[C]_\infty$. Equation 17 then gives

$$K_{1,n} = \frac{1}{[C]_\infty} \exp\left\{\frac{-(\Delta G_{1,n}^{\text{vol}} + \Delta G_{1,n}^{\text{surf}})}{k_B T}\right\} \quad (18)$$

In the framework of equilibrium theory we assume all particles with $n < p$ monomer units have condensation reactions that are in equilibrium and for $n > p$, $[C_n] = 0$. Now we consider all the reactions that occur simultaneously at equilibrium. These are $C + C \rightleftharpoons C_2$, $C_2 + C \rightleftharpoons C_3$, $C_{p-1} + C \rightleftharpoons C_p$ and so forth. The sum of these reactions is



where p units condense to form a critical nucleus. The equilibrium constant for the formation of a critical nucleus (eq 19) is simply the product of the equilibrium constants for all the sequential reactions that result in the production of a critical nucleus:

$$K_{\text{nuc}} = \prod_{n=1}^{p-1} K_{1,n} \quad (20)$$

From eq 19 it follows that $[C_p] = K_{\text{nuc}}[C]^p$. Using eqs 18 and 20 we may then form an expression for the concentration of critical clusters, $[C_p]$, as

$$[C_p] = \frac{[C]^p}{[C]_\infty^{p-1}} \exp\left\{\frac{-(\Delta G_{1,p}^{\text{vol}} + \Delta G_{1,p}^{\text{surf}})}{k_B T}\right\} \quad (21)$$

The rate of nucleation is given by the rate of formation of the first stable particle, C_{p+1} :

$$R_{\text{nuc}} = k_{1,p}[C][C_p] \quad (22)$$

The maximum value of $k_{1,p}$ is the diffusional collision frequency, which is given by

$$k_{1,p} = 8\pi r_m D N_A \quad (23)$$

where N_A is the Avogadro constant and r_m is the effective radius of the monomer as extracted from the molar volume, V_m . The Gibbs free energy of the surface, ΔG^{surf} , is given by $4\pi r^2 \gamma$ and the volume free energy, ΔG^{vol} , by $4/3\pi r^3 \Delta G_v$ with $\Delta G_v = -RT/V_m \ln S$. The corresponding energy barrier yields the required critical radius, r_{crit} , for nucleation. Equations 21, 22, 23, and 11 then give the rate of formation:

$$R_{\text{nuc}} = 8\pi r_m D N_A S^{p+1} [C]_\infty^2 \exp\left\{\frac{-(4\pi r_{\text{crit}}^2 \gamma)}{3k_B T}\right\} \quad (24)$$

We now introduce a coagulation coefficient, u , to account for the coagulation of subcritical nuclei. Here u may take values between 0 and 1 and acts as a scaling factor, which balances the kinetic and thermodynamic aspects of the nucleation rate. It accounts for the probability that in addition to the stepwise addition of monomer units, nucleation may proceed via the coagulation of dimers and trimers, etc. with each other, as well as with the monomer. Thus, eq 19 becomes



Equation 25 represents the number averaged (u) reaction pathway to the formation of a critical nucleus. It should be noted that eq 25 and its implications are only valid for weakly coagulating systems ($u \gtrsim 0.5$). The boundary condition is that $1/u \leq p$. At equilibrium the concentration of monomers and dimers ($n = 1, 2$), etc. is extremely high compared to cluster species with higher n values. Given that the probability of coagulation decreases with both decreasing concentration and increasing size of the coagulants, the coagulation rate decreases rapidly as n is increased from $1 \rightarrow p$. As such, an

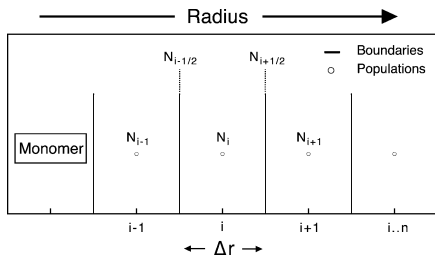


Figure 2. Uniform grid configuration, where $r_i = i\Delta r$ denotes the radius of the i th population (bin). Matter flows into or out of the i th bin according to fluxes $\Gamma_{i-1/2}N_{i-1/2}$ and $\Gamma_{i+1/2}N_{i+1/2}$ at the faces of the bin.

implicit assumption is that coagulation does not significantly modify the thermodynamic barrier to nucleation. Noting that $p = (r_{\text{crit}}/r_m)^3$, we may write the final expression for the nucleation rate, determining the number of moles of critical clusters formed per unit volume per unit time:

$$R_{\text{nuc}} = 8\pi r_m D N_A S^{p+1} [C]_{\infty}^2 \exp\left\{\frac{-(4\pi r_m^2 p^{2/3} \gamma)}{3k_B T}\right\} \quad (26)$$

For plots of the nucleation rate as a function of various reaction parameters see the Supporting Information. The only remaining variable to evaluate is the nucleation distribution function, $g(r)$. Here we have assumed a thermalized distribution (Gaussian) around the critical radius with a fwhm $\approx k_B T$. Although we would expect many more dimers and trimers, etc. than critical nuclei, test runs revealed that changing the form of the initial stationary distribution function, $g(r)$, had a minimal effect on the outcome of the simulations (see the Supporting Information for details). We attribute this insensitivity to the extremely fast dissolution rates of particles with radii below the critical radius.

Ensemble Dynamics. Initially, at $t = 0$ a fixed amount of monomer is added (injected). The system is then assumed to be closed in that no additional monomer is added or removed subsequently. The conservation equation giving mass balance is

$$Sl_{t=t_1} = Sl_{t=t_0} - Q \int_0^{\infty} r^3 \{n(r, t_1) - n(r, t_0)\} dr \quad (27)$$

where $n(r, t)$ is the number density function of particles of radius r . Equation 27 describes the evolution of free monomer from any time $t = t_0$ to any other time $t = t_1$. The constant Q is given by

$$Q = \frac{4\pi\rho}{3M_W V_{\text{tot}} [C]_{\infty}} \quad (28)$$

where ρ is the density of the bulk material, M_W is its monomeric molecular weight and V_{tot} is the volume of the reaction solution.

Numerical Implementation

We now consider an ensemble of particles with a range of radii. To model the evolution of this ensemble we discretise the distribution of radii into P bins. Figure 2 displays a schematic of the grid configuration used in this work. Equation 27 then gives

$$Sl_{t=t_1} = Sl_{t=t_0} - \sum_{i=1}^P Q r_i^3 (N_i|_{t=t_1} - N_i|_{t=t_0}) \quad (29)$$

where N_i is equal to the number of particles in the i th bin at a given time and r_i is the radius of such particles (see Figure 2). To model the dynamics of the ensemble we solve the coupled system given by eqs 9, 26, and 29. This then accounts for the change in supersaturation (free monomer) as a function of time.

To simulate growth and nucleation we use a standard population balance model (PBM). The continuity equation giving mass balance is

$$\frac{\partial N}{\partial t} + \frac{\partial \Gamma N}{\partial r} = R_{\text{nuc}} g(r) \quad (30)$$

Equation 30 is an advection equation (with a source) for the frequency N of the population. The advection flux of N is ΓN where Γ is the velocity given by the instantaneous growth rate. The source term $R_{\text{nuc}} g(r)$ is the rate of production of new nuclei given by the nucleation rate, R_{nuc} , and its distribution function $g(r)$. Equation 30 is solved numerically by an explicit time-stepping procedure using the following discretization for the i th bin ($i = 1, 2, \dots, P$) at time $t = k\Delta t$ ($k = 0, 1, 2, \dots$):

$$\frac{N_i^{(k+1)} - N_i^{(k)}}{\Delta t} + \frac{(\Gamma N)_{i+1/2}^{(k)} - (\Gamma N)_{i-1/2}^{(k)}}{\Delta r} = R_{\text{nuc}}^{(k)} g(r_i) \quad (31)$$

where Δt is the time step. The update of $N_i^{(k)}$ to $N_i^{(k+1)}$ is performed in two steps. We first nucleate some particles to arrive at an intermediate value, \tilde{N}_i , for the distribution, which is given by

$$\tilde{N}_i = N_i^{(k)} + \Delta t R_{\text{nuc}}^{(k)} g(r_i) \quad (32)$$

The new array of N at time level $(k + 1)$ may now be expressed as

$$N_i^{(k+1)} = \tilde{N}_i - \frac{\Delta t}{\Delta r} \{(\Gamma N)_{i+1/2}^{(k)} - (\Gamma N)_{i-1/2}^{(k)}\} \quad (33)$$

\tilde{N}_i can be evaluated directly as can $\Gamma_{i\pm 1/2}^{(k)}$. However, we need to interpolate $N_{i\pm 1/2}^{(k)}$ at the bin faces from neighboring values of N at the bin centers. The interpolation scheme chosen should generate minimal numerical (false) diffusion. Numerical diffusion can completely destroy the solution accuracy when physical diffusion is absent (the present case) or small, especially in the presence of steep gradients, as can occur here.

A MUSCL (Monotone Upstream-centered Schemes for Conservation Laws) interpolation scheme, as pioneered by Van Leer et al.,^{30,31} provides a powerful resolution to the problem of suitably evaluating $N_{i\pm 1/2}$. It combines higher-order differencing with flux limiting to ensure that the solution remains bounded. Higher order schemes without flux limiting can develop oscillations even though they are formally more accurate when assessed by Taylor series expansion. Flux limiters prevent nonphysical oscillations from occurring near regions of steep gradients. Here we use second order upwind differencing with a Van Leer flux limiter^{30,31} as follows

$$N_{i-1/2} = N_i - \frac{1}{2} \Psi \left(\frac{\nabla_i^-}{\Delta_i^+} \right) \Delta_i^+ \quad \Gamma_{1-1/2} < 0 \quad (34)$$

$$N_{i+1/2} = N_i + \frac{1}{2} \Psi \left(\frac{\Delta_i^+}{\nabla_i^-} \right) \nabla_i^- \quad \Gamma_{1+1/2} > 0 \quad (35)$$

where the Van Leer limiter function $\Psi(\chi)$ is given by

$$\Psi(\chi) = \frac{\chi + |\chi|}{1 + \chi} \quad (36)$$

and the differences, Δ_i^+ and ∇_i^- , are defined as

$$\begin{aligned} \Delta_i^+ &= N_{i+1} - N_i \\ \nabla_i^- &= N_i - N_{i-1} \end{aligned} \quad (37)$$

A comprehensive account of the properties and action of flux limiter functions can be found elsewhere.³¹

Stability and Accuracy of the Numerical Scheme. We tested the accuracy of the flux-limiting scheme by applying it to the uniform advection of both Gaussian and step-functions. These function profiles should remain unchanged during pure advection. Detailed results from the test simulations are provided in the Supporting Information. Briefly, we confirmed that the second-order flux-limited scheme used here accurately preserves the shape of the Gaussian and step-functions during advection. In contrast, advection based on simple, first-order upwinding produced final profiles that were artificially broadened by numerical diffusion. This is very important to avoid in the modeling of nanocrystals where interpretation of the results of a given simulation relies heavily on the full width at half-maximum of the distribution.

The numerical scheme implemented here is explicit, and so the *Courant condition*³² must be satisfied to ensure stability:

$$\frac{|\Gamma| \Delta t}{\Delta r} \leq 1 \quad (38)$$

This ensures that mass is not advected through more than one bin in a single time step. Throughout this report we set $\Delta r = 0.3 \text{ \AA}$. This value was chosen as it provides accurate tracking of single atoms (monomer units) in the limit $r \rightarrow 0$. Test runs confirmed that the choice of Δr between 0.05 and 5 \AA had no effect on the outcome of the simulation. For all of the simulations reported here Δt was set to ensure eq 38 was satisfied for all moments of the simulation. Typically, $\Delta t = 1 \times 10^{-3}$ (in the reaction limit) and 1×10^{-6} (in the diffusion limit). Importantly, Courant numbers were always ≤ 0.5 . For a schematic outline of the algorithm see the Supporting Information.

Simulations

Growth-Only Simulations. Prior to developing an understanding of coupled nucleation and growth it is important to understand the effects of growth only on an evolving distribution. Consequently, we begin by examining only the growth of nanocrystals. To accomplish this the source term is removed from the simulation and an artificial distribution of NCs is inserted at $t = 0$. Throughout the following simulations a

Gaussian with a mean radius of $1 \times 10^{-9} \text{ m}$ and a standard deviation (SD) of $\sim 10\%$ was employed. Both the mean size and the SD of the initial PSD approximate known values obtained at the end of the nucleation phase during NC synthesis.^{3,33,34}

Growth in the Diffusion and Reaction Limits. The following simulations, outlined in Figures 3, 4, and 5 were designed to uncover the effects of surface energy (γ) on the evolution of a series of PSDs in both the diffusion and reaction limits. These simulations were accomplished with $S = 500$, $D = 1 \times 10^{-12} \text{ m}^2 \text{ s}^{-1}$, $[C]_\infty = 1 \times 10^{-2} \text{ mol m}^{-3}$, $T = 503 \text{ K}$, and $60 \text{ }\mu\text{M}$ nanocrystals.

Diffusion-Limited Growth. Figure 3 shows the concentration of NCs (A), %SD (B), mean radius (C), and supersaturation (D) as a function of time for increasing values of γ in the range $0.05\text{--}0.3 \text{ J m}^{-2}$ under diffusion-limited conditions ($\xi = 1 \times 10^{-3}$). For clarity and brevity in the explanation of these results the discussion is first restricted to the growth dynamics of those NCs with $\gamma = 0.2 \text{ J m}^{-2}$, followed by a discussion of the dynamics of those NCs with differing surface energies. For the case where $\gamma = 0.2 \text{ J m}^{-2}$ NC evolution has been divided into three regimes relative to the supersaturation dynamics as indicated by the vertical dotted lines in each of the plots. Specifically, these lines separate the reaction into times when S is in rapid decline, remaining approximately constant and finally in slow decline. It is important to note that these three regimes are seen for all NC systems investigated here. For clarity, dividing lines have only been drawn for the system where $\gamma = 0.2 \text{ J m}^{-2}$. We now discuss the reaction dynamics in each of these regimes for $\gamma = 0.2 \text{ J m}^{-2}$. Inspection of Panel C reveals that between $100 \text{ }\mu\text{s}$ and 30 ms the NCs grow at an approximate rate of 40 nm s^{-1} to reach a size of $\sim 3.22 \text{ nm}$. During this time S is in rapid decline, the concentration of NCs remains constant, and the PSD narrows from a SD of $\sim 10\%$ to a minimum of $\sim 5\%$. Henceforth, this time period will be referred to as the fast growth phase. Between 30 and 800 ms the mean radius remains constant as does the [NCs] and S . Hereafter, this time period will be referred to as the quasi-equilibrium phase of the reaction. Notably, during this time the PSD is rapidly broadening. At around 800 ms the supersaturation begins to drop again and the reaction enters a new phase. This phase is signified by a decrease in the NC concentration and an increase in the mean size of the NCs. As evident from the small changes in S during the final phase (800 ms to 60 s), growth of the NCs is almost solely governed by monomer provided by the dissolution of the smallest crystallites within the evolving PSD. Consequently, we label this time period the Ostwald ripening phase of the reaction. It should be noted that as the NCs begin to ripen the SD begins to plateau. Further rapid broadening of the PSD is prevented by the fast dissolution of small NCs and as such the SD increases only slowly between ~ 1 and 60 s .

Upon comparing simulations with surface energies between 0.05 and 0.3 J m^{-2} some interesting trends are revealed. First, from inspection of the data for $t \lesssim 100 \text{ ms}$ in Panel C it can be seen that, independent of their initial γ , the NCs grow at the same rate and to the same final size. These results are indicative of diffusion limited growth (at constant [NCs]) where the growth rate is determined solely by the rate at which monomer can reach the surface and independent of those factors that alter the surface reactivity of the particle, such as the surface energy. Inspection of Panel D reveals that the concentration of monomers present in solution once the reaction has reached quasi-equilibrium increases with increasing surface energy, with an

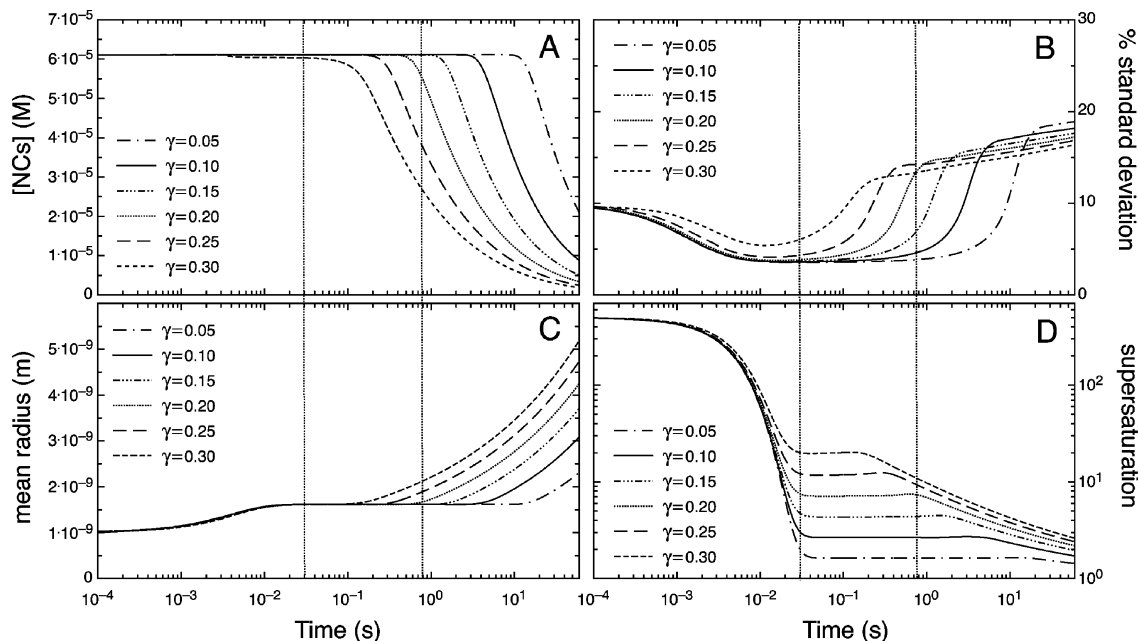


Figure 3. Nanocrystal concentration (A), standard deviation (B), mean radius (C), and supersaturation (D) as a function of time for NC growth under diffusion limited conditions ($\xi = 1 \times 10^{-3}$) with increasing surface energies. The vertical lines in each of the plots divide the reaction where $\gamma = 0.2 \text{ J m}^{-2}$ into three phases in accordance with its supersaturation dynamics. Specifically, these are the fast growth phase, the quasi-equilibrium phase, and the Ostwald ripening phase.

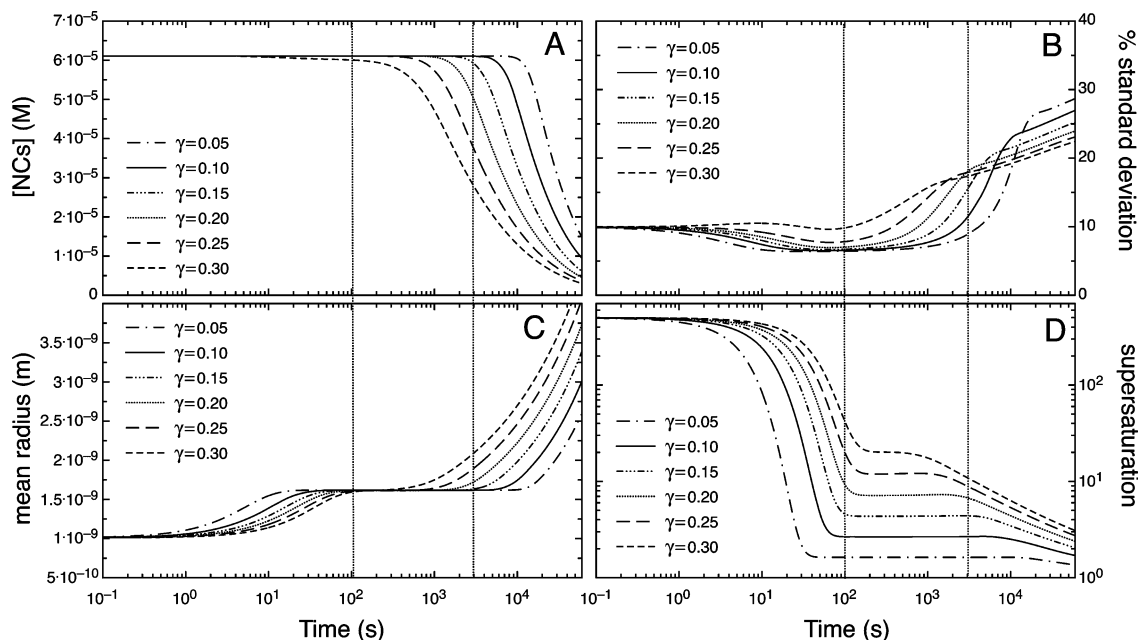


Figure 4. Nanocrystal concentration (A), standard deviation (B), mean radius (C), and supersaturation (D) as a function of time for NC growth under reaction limited conditions ($\xi = 2000$) with increasing surface energies. The vertical lines in each of the plots divide the reaction where $\gamma = 0.2 \text{ J m}^{-2}$ into three phases in accordance with its supersaturation dynamics. Specifically, these are the fast growth phase, the quasi-equilibrium phase, and the Ostwald ripening phase.

order of magnitude more monomer required to prevent the dissolution of particles with $\gamma = 0.3 \text{ J m}^{-2}$ compared to NCs whose $\gamma = 0.05 \text{ J m}^{-2}$.

The time at which the NCs exit the quasi-equilibrium phase and begin to grow again is determined by their surface energy. This is because the surface energy governs the time scale on which broadening (and thus ripening) of the PSD occurs. Comparison of Panels A and B reveals that once the PSDs have reached a SD of $\sim 12\%$ they begin to ripen. As distributions with higher surface energies undergo less narrowing during the fast growth phase they reach this critical SD earlier and thus

begin to ripen first. As a consequence, the time scale of the quasi-equilibrium phase is shortened from 10 s to 90 ms upon increasing γ from 0.05 to 0.3 J m^{-2} . Finally, from Panels A, B, and C it can be seen that increasing γ results in lower concentrations of NCs having larger sizes and narrower distributions at the end of the reaction.

Reaction-Limited Growth. Figure 4 depicts results using the same parameters as those used for simulation under diffusion control. However, ξ was raised by ~ 6 orders of magnitude to a value of $\xi = 2000$ such that growth proceeded under reaction-limited conditions. Similar trends are observed in the SD and

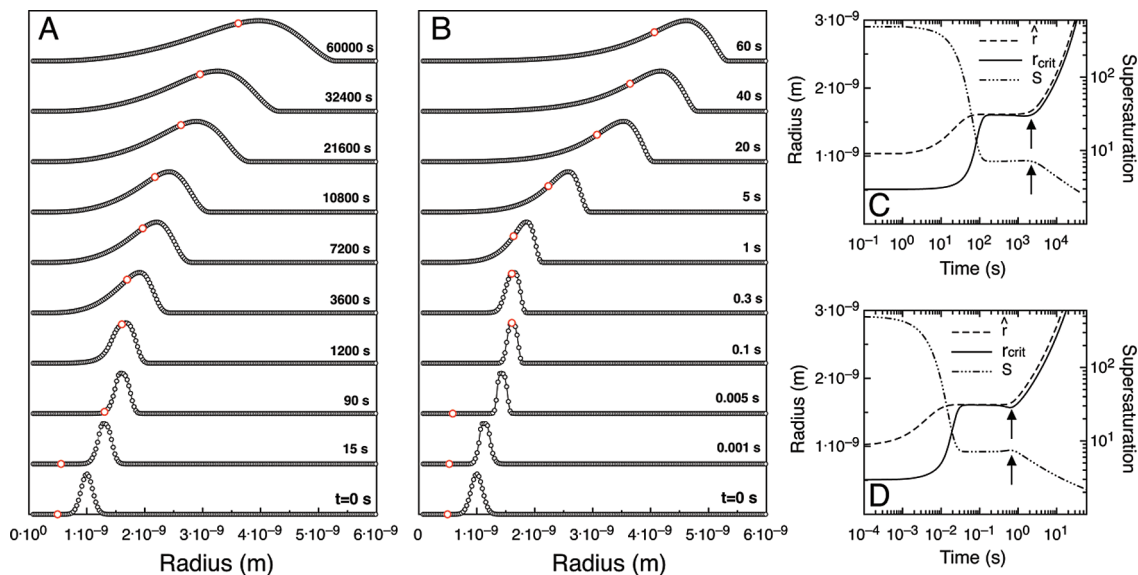


Figure 5. PSDs as a function of reaction time in both the reaction (A) and diffusion (B) regimes. (C and D) Corresponding temporal dynamics of the critical radius r_{crit} , mean radius \hat{r} , and supersaturation S for both the reaction and diffusion-limited simulations, respectively.

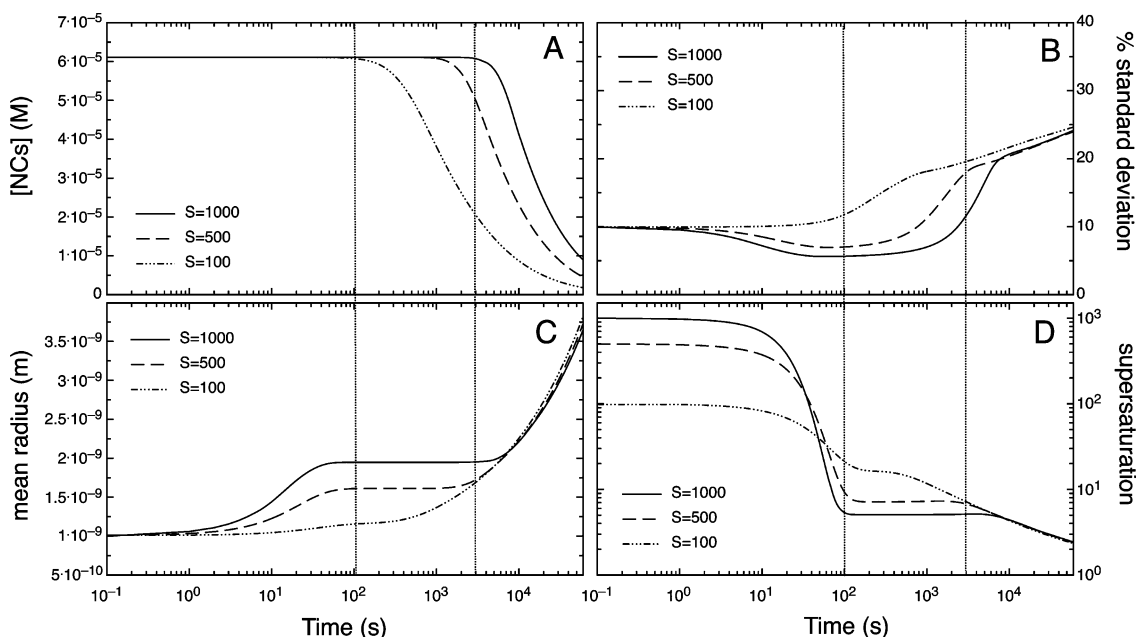


Figure 6. Nanocrystal concentration (A), standard deviation (B), mean radius (C), and supersaturation (D) as a function of time for NC growth under reaction limited conditions ($\xi = 2000$) with increasing initial supersaturations. The vertical lines in each of the plots divide the reaction where $S = 500$ into three phases in accordance with its supersaturation dynamics. Specifically, these are the fast growth phase, the quasi-equilibrium phase, and the Ostwald ripening phase.

[NCs] over time as those seen for the diffusion limited simulations, although the time scale of these trends is vastly longer. The greatest differences in reaction kinetics between the diffusion and reaction limited regimes are seen by analysis of the mean radius and S as a function of time, shown in Panels C and D, respectively. Contrary to the diffusion limited case the growth rate of the NCs during the fast growth phase depends strongly on the surface energy of the NCs. The fastest growth rates are seen for NCs with the lowest γ , and these decrease as γ is increased. As strongly binding ligands lower γ to a greater extent than weaker binding ligands, we expect slower rates of growth for lower values of γ , contrary to what is observed. This is understood as in addition to lowering γ , the presence of strong binding ligands in solution must also slow the surface reaction rate (increase ξ). The surface half-life of strong binding ligands is much greater than weaker binding species and as a conse-

quence they are able to physically inhibit monomer adsorption to a greater extent. Therefore, γ and ξ are intrinsically linked and when modeling the evolution of a PSD simulating different types and concentrations of adsorbates in solution, appropriate concomitant modifications to *both* γ and ξ need to be made.

Compared to diffusion-limited growth, the standard deviations of the PSDs under reaction control were seen to broaden to a greater extent during the quasi-equilibrium phase. On average, the final distributions had standard deviations about 5% greater than those grown under diffusion control. Finally, from the overall time scale of the reactions we may conclude that NC growth must proceed under highly reaction-controlled kinetics. To reinforce this point it should be noted that the diffusion coefficient used during these simulations was already at a lower limit for values appropriate to small precursor species (molecules).³⁵ Despite the low diffusion coefficient, the fast growth

phase under diffusion limited conditions still took place on a time scale of milliseconds. Simulations performed using a diffusion coefficient of $1 \times 10^{-10} \text{ m}^2 \text{ s}^{-1}$ under the same extent of diffusion control ($\xi = 1 \times 10^{-3}$) resulted in the growth of NCs from 1 to 3 nm in under 1 ms, which is several orders of magnitude too fast compared to experimentally observed NC growth rates.^{3,5,29}

Summary of Diffusion- and Reaction-Limited Growth. Figure 5 shows the evolution of the PSDs in both the reaction (A) and diffusion (B) limits with $\gamma = 0.2 \text{ J m}^{-2}$. The white dots on each of the curves indicates the critical radius (zero growth radius) of the system at that moment. Panel A shows that under reaction control the fwhm of the distribution remains constant at early reaction times ($t \lesssim 100 \text{ s}$). During this period the NCs grow from 2 to 3 nm. As a result of monomer consumption the critical radius (r_{crit}) approaches the mean radius (\bar{r}) of the PSD, which triggers broadening and eventual ripening of the nanoparticle ensemble. Panel B displays various snapshots of the PSD under diffusion control. Contrary to the reaction-limited case the fwhm of the distribution narrows during the early stages of NC growth. We submit here that this observation of “narrowing” may be a contributing factor to the misinterpretation that NC growth proceeds under diffusion limited kinetics. Finally, comparison of the distributions at the termination of the simulations (Panel A, 60 000 s; Panel B, 60 s) reveals the PSD to be narrower when it has evolved under diffusion limited conditions.

Analysis of Panels C and D reveal that during the quasi-equilibrium phase r_{crit} and \bar{r} adopt similar values. Toward the very end of this phase, dissolution of the smallest NCs begins to provide monomer to the reaction solution. However, not enough monomer is provided to reinstate net NC growth. As such, S gradually increases (only by fractions of a unit) and a concomitant decrease in r_{crit} is observed (see arrows in Panels C and D). Eventually the “equilibrium” between r_{crit} and \bar{r} is broken as a result of S having increased to a value that allows for net growth of the PSD. After this period traditional Ostwald ripening ensues, which is exemplified by an increase in the mean radius and SDs of the PSDs.

Interestingly, the value of the supersaturation during the quasi-equilibrium phase is the same in both limits. As the size of the NCs are the same during this phase in each of the limits, we may infer that the value of S corresponds to the NC solubility. In support of this interpretation Figures 3 and 4 show that the value of S during the quasi-equilibrium phase increases with increasing γ , as NCs with high surface energies require more monomer to prevent their dissolution.

Effect of Initial Supersaturation on Reaction-Limited Growth. The simulations outlined above clearly prove that NC growth occurs under reaction limited conditions. Consequently, further simulations have been directed solely toward a deeper understanding of NC growth in the reaction limit. The following simulations were designed to expose the effects of the initial supersaturation on the evolution of a PSD. The same parameters were used as those outlined in the previous section with $\gamma = 0.2 \text{ J m}^{-2}$. Panel C shows that between 0 and 100 s the growth rate is strongly dependent on the supersaturation in solution, with faster growth rates occurring in solutions with higher initial supersaturations. Panel A shows that the onset of ripening occurs at earlier times in systems with a lower initial S . Panel B indicates that, similar to lowering γ , increasing S results in greater initial reductions to the SD and a lower minimum at the onset of quasi-equilibrium. By $\sim 10\,000 \text{ s}$ all the SDs have converged to a value of $\sim 24\%$.

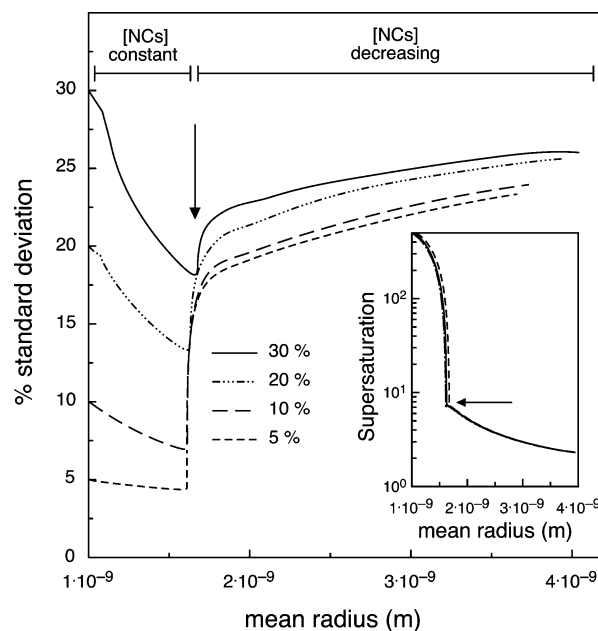


Figure 7. Plot of the percent standard deviation as a function of mean radius for different initial standard deviations (distribution widths). The supersaturation in solution as a function of mean radius (inset). The arrows in both plots signify the change in growth dynamics from growth governed by monomer accretion to growth dominated by the rate of ripening within the system.

Inspection of Panel C and D reveals convergence of \bar{r} and S at times longer than 10 000 s. However, the particle concentrations do not converge, with higher NC concentrations evident in systems with higher initial S values. These data further corroborate the observation that at longer reaction times the evolution of the PSDs are no longer governed by the supersaturation in solution but rather by ripening. Finally, it is of great importance to note that during the quasi-equilibrium phase S adopts larger values for systems with smaller average crystal sizes. As discussed in the previous section the value of S at quasi-equilibrium is directly related to the NC solubility. From Panels C and D it may therefore be calculated that NCs with sizes 3.8, 3.2, and 2.4 nm (with surface energies of 0.2 J m^{-2}) are in equilibrium with monomer concentrations of 51, 72, and 162 μM , respectively. These numbers are in reasonable agreement with those found experimentally by Qu et al.⁴

Effect of Initial Standard Deviation on Reaction-Limited Growth. To examine the effect of the initial SD on the evolution of NCs we again assume the same values for the variables and constants outlined in the previous sections ($\gamma = 0.2 \text{ J m}^{-2}$ and $S = 500$) and vary the initial SD from 5 to 30%. Figure 7 is a plot of the SD as a function of \bar{r} . Plotting the SD as a function of \bar{r} highlights changes to the SD as a direct consequence of NC growth, independent of the time scale of either broadening or narrowing. The data show that regardless of their initial standard deviations, which span 25%, the standard deviations at the termination of the simulation span a range of only $\sim 3\%$. However, the dynamics of these changes depend upon the initial SD. For growth between 2 and 3.2 nm the [NCs] remains constant and greater extents of narrowing are observed for higher initial SDs. During the ripening phase (whose onset is denoted by the arrows in Panels A and B) NCs with an initial SD of 30% broaden by only $\sim 7\%$ while those distributions with initial SD values of 5% broaden by 19%. The initially narrow distributions must broaden to a greater extent before a significant number of NC reach the left boundary (dimers) and disappear,

subsequently providing the monomer necessary to resume NC growth. The inset shows that, independent of their initial SDs, when the mean size reaches ~ 3.2 nm ($\bar{r} \approx 1.6$ nm) the rapid decline in supersaturation ceases. Further growth decreases S only by a factor of 4 despite the fact that it requires orders of magnitude more monomer to grow a given number of NCs from 3.2 to 8 nm compared to 2–3.2 nm. These data further support of the conclusion that after the quasi-equilibrium phase NC growth is dominated by the rate of Ostwald ripening.

Comparisons with LSW and Wagner Theories. For diffusion- and reaction-controlled coarsening, stationary size distributions have been predicted by Lifshitz, Slyosov, and Wagner (LSW)¹⁰ and Wagner,³⁶ respectively. For diffusion limited coarsening the stationary distribution function $W(u)$, where $u = r/r_{\text{crit}}$, is given by

$$W(u) = \begin{cases} \frac{(3^4 e^{5/3}) u^2 \exp[-1/(1 - 2u/3)]}{[(u + 3)^{7/3} (1.5 - u)^{11/3}]} & \text{if } 0 < u < 1.5 \\ 0 & \text{otherwise} \end{cases} \quad (39)$$

For reaction-limited coarsening:

$$W(u) = \begin{cases} 2^7 3 u (2 - u)^{-5} \exp\left[\frac{-3u}{(2 - u)}\right] & \text{if } 0 < u < 2 \\ 0 & \text{otherwise} \end{cases} \quad (40)$$

Figure 8 shows the results of the numerical simulations performed in the reaction ($\xi = 2000$) and diffusion ($\xi = 1 \times 10^{-3}$) limits. These results are plotted alongside the corresponding stationary distributions as predicted by the LSW and Wagner models, eqs 39 and 40, respectively. Both numerical simulations were conducted with the following parameters: $T = 503$ K, $V_m = 3.2996 \times 10^{-5} \text{ m}^3 \text{ mol}^{-1}$, $D = 1 \times 10^{-12} \text{ m}^2 \text{ s}^{-1}$, $[C]_\infty = 1 \times 10^{-2} \text{ mol m}^{-3}$ and $\gamma = 0.3 \text{ J m}^{-2}$. At the termination of each simulation changes to the SD and monomer consumption rates were $\leq 1 \times 10^{-3}\%$ and $\ll 1 \text{ atom s}^{-1}$ in both limits, respectively, indicating that in each case the distributions were at their asymptotic limits.

Figure 8 shows that in both limits the PSDs (dotted lines) are narrower than their respective predicted stationary distributions (solid lines). This is understood as only first-order terms in the expansion of the Gibbs–Thomson equation were used in the derivation of eqs 39 and 40. Retaining the full exponential term contributes to rapid dissolution of those NCs whose $r < r_{\text{crit}}$, which is accentuated for nanosized particles.^{15,22} Accounting for this rapid dissolution results in final PSDs with lower SDs than predicted by the LSW and Wagner models. In order to test this hypothesis the simulations were repeated using growth equations that retained only the first term in the Taylor expansion of the Gibbs–Thomson approximation (see eq 7). These simulations revealed much closer agreement between the numerical asymptotic and stationary distributions in both limits (dashed curves). These results place in doubt the validity of the LSW and Wagner models for colloids of nanocrystals.

Nucleation and Growth Simulations. Having established the effects of various parameters on the growth of NCs we now focus on the more complex dynamics of simultaneous nucleation and growth. Great care was taken to ensure the simulation conditions were as close as possible to typical experimental conditions used to synthesize NCs. Typical preparations of NCs

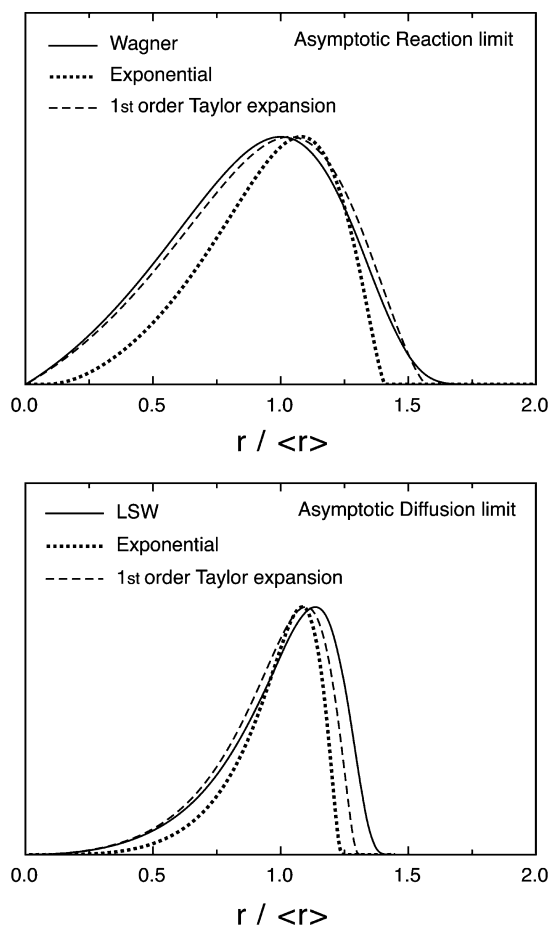


Figure 8. (Top) Stationary size distribution as predicted by Wagner (solid line) and the asymptotic numerical distributions obtained from simulations using the full exponential growth term (dotted line) and first-order Taylor-expanded approximation (dashed line). (Bottom) Stationary size distribution as predicted by LSW theory (solid line) and the asymptotic numerical distributions obtained from simulations using the full exponential growth term (dotted line) and first-order Taylor-expanded approximation (dashed line).

employ between 10 and 50 mol m^{-3} of monomer.^{3,37,38} Assuming $[C]_\infty$ to be on the order of 0.001 mol m^{-3} ($1 \mu\text{M}$ monomer in equilibrium with an infinitely flat surface; $\sim 99.99\%$ monomer conversion) then initial supersaturations of ca. 40 000 are reasonable. However, for the following simulations $[C]_\infty$ was set to 0.004 mol m^{-3} and consequently S was varied between 8000 and 14 000 ($32\text{--}56 \text{ mol m}^{-3}$ monomer). The temperature during the simulation was adjusted according to a mathematical fit of the temperature drop profiles recorded during the synthesis of CdSe outlined elsewhere.³ For reference, the experimental and modeled temperature drop profiles are displayed in Figure 10. A prominent issue when modeling NC nucleation and growth is the inability to confidently assign accurate values to γ . At present, to the best of the authors' knowledge, no experimental data exist on the surface energy of NCs. This is likely due to the complex nature of γ , which depends on particle size, temperature, ligand type, and concentration. Estimations of γ using the assumptions of equations outlined by Sugimoto¹² and Bullen et al.³⁷ under the reaction conditions described here yield values for $\gamma \sim 0.5 \text{ J m}^{-2}$. Given that the nucleation and growth of most NCs typically occurs at high temperatures in the presence of ligands that form highly soluble complexes with the monomer the value assigned to γ must surround or be somewhat higher than 0.5 J m^{-2} . For the following simulations γ was set at 1.1 J m^{-2} . To ensure growth on a time scale

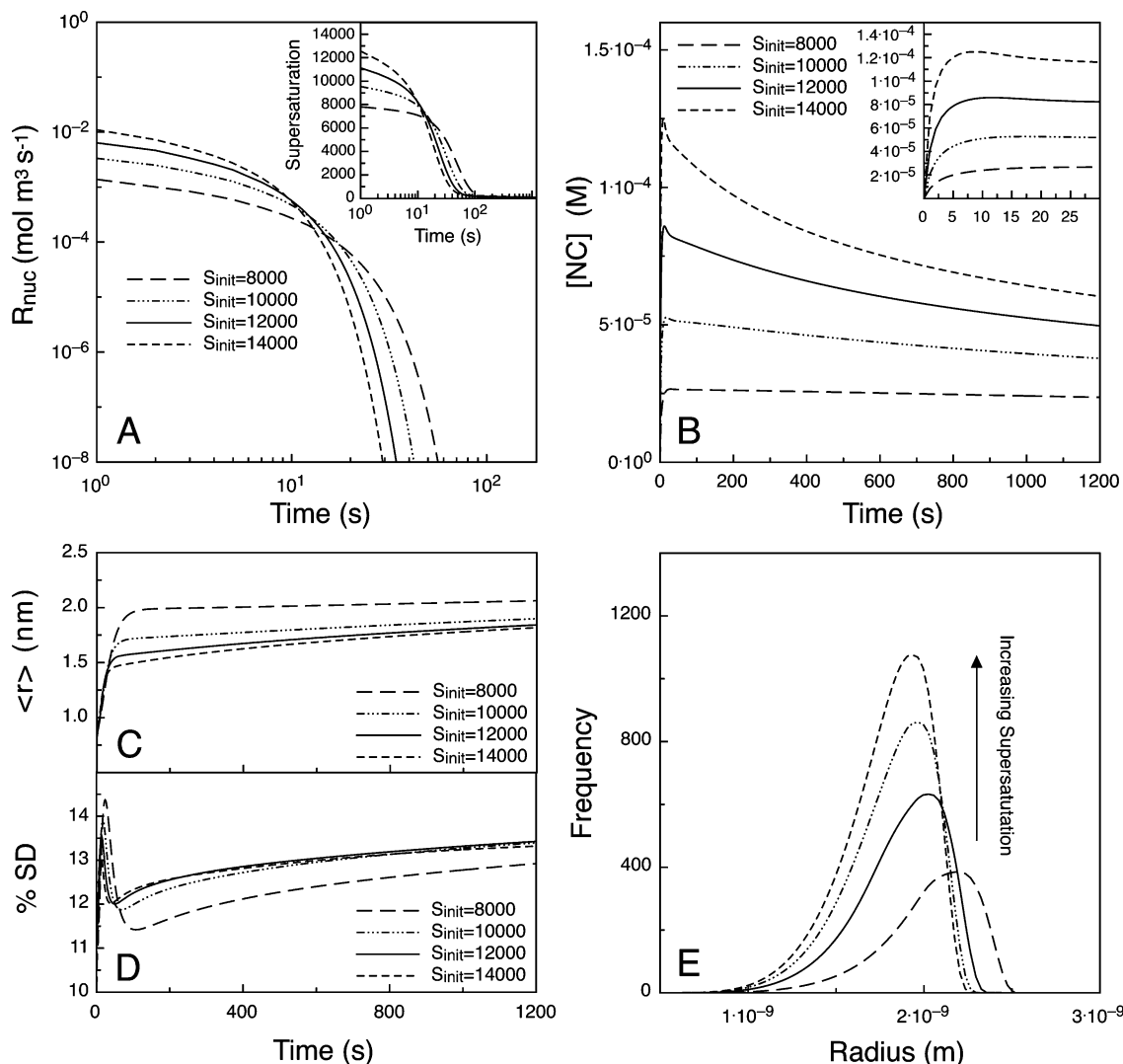


Figure 9. (A) R_{nuc} as a function of time (the inset shows the supersaturation dynamics). The remaining panels display the (B) [NC], (C) mean radius, \bar{r} , and (D) SD as a function of time. (E) Plot of the unscaled PSDs at the termination of the reaction.

appropriate to normal NC synthesis ξ was set at 1×10^5 . A monomer diffusion coefficient of $5 \times 10^{-11} \text{ m}^2 \text{ s}^{-1}$ was used, which is similar to measurements of small molecules.³⁵ The remaining constants were assigned values specific to CdSe and CdSe related syntheses, namely $V_m = 1.65 \text{ mol m}^{-3}$ (half the molar volume of a CdSe dimer), $T_{inj} = 573 \text{ K}$, $T_{gr} = 503 \text{ K}$, the radius of the monomer $r_m = 1.87 \times 10^{-10} \text{ m}$. A coagulation coefficient of 0.48 was also employed. Unless otherwise stated, the above list of parameters are assumed.

Effect of Initial Supersaturation. In this section the effect of the initial supersaturation (S_{init}) on the nucleation and growth of nanocrystals is addressed. Figure 9A displays the nucleation rate as a function of time on a log–log scale. It can be seen that lower initial supersaturations lead to lower initial nucleation rates. $S_{init} = 8000$ cedes initial rates of $1.4 \times 10^{-3} \text{ mol m}^{-3}$ ($1.4 \text{ } \mu\text{M s}^{-1}$) while $S_{init} = 14000$ imparts initial rates approximately eight times higher at $1.1 \times 10^{-2} \text{ mol m}^{-3}$ ($11 \text{ } \mu\text{M s}^{-1}$). Inspection of Panel B reveals that, in accordance with increasing initial nucleation rates, higher values of S_{init} result in the formation of increasing numbers of NCs. Upon raising S_{init} from 8000 to 14 000 the maximum concentration of nuclei increases from 26 to 125 μM . Clearly, the rate of monomer depletion is proportional to the number of nuclei formed with an increased number of growth centers containing and removing larger amounts of monomer from the solution per unit of time.

As such, having nucleated fewer NCs the nucleation rate for the simulation with $S_{init} = 8000$ is seen to remain higher for longer periods of time compared to systems with larger values of S_{init} . Specifically, the nucleation phase lasts around twice as long for $S_{init} = 8000$ compared to $S_{init} = 14000$. It should be noted that once R_{nuc} dropped below $1 \times 10^{-8} \text{ mol m}^{-3} \text{ s}^{-1}$ (10 pM s^{-1}) nucleation was considered complete.

Upon raising S_{init} from 8000 to 14 000 the mean size of the nuclei formed in the first nucleation event decreased from 8.54 to 8.15 Å. A decrease in initial nuclei size arises due to the increased thermodynamic stability of smaller NCs in the presence of higher initial supersaturations. Analysis of Panel B highlights the competing kinetic and thermodynamic processes that occur during the early stages of NC formation and growth. Although high S_{init} values kinetically favor nucleation, the nuclei that are formed are not necessarily thermodynamically stable. To highlight this we note that ripening is seen to begin directly following the end of the nucleation phase where $S_{init} = 14000$ despite the higher monomer saturation levels at the end of nucleation compared to the reaction where $S_{init} = 8000$ (see insets Panels A and B). From these data we may infer that ripening is also occurring *during* nucleation; however, it is obscured by the net formation of particles. Close inspection of the early times in Panel B (inset) reveal that once the [NCs] has reached its maximum, $[NC]_{max}$, extremely fast ripening

begins, which is more pronounced in systems with larger numbers of NCs.

A direct correlation between the nucleation and growth rates is observed by comparing the data of Panels B and C, respectively. Although all the growth rates are somewhat similar during the nucleation phase, having nucleated fewer NCs, the growth rate of NCs in systems with lower S_{init} values remains higher for longer periods. Due to the fast continual growth of the nuclei to larger sizes, they significantly distance themselves from the critical radius of the system. Thus, almost no ripening is observed for the case where $S_{\text{init}} = 8000$. At longer times the ripening rate is seen to plateau in all systems. The combined data of Panels A, B, and C show that the initial supersaturation determines the number of nuclei formed, the early time growth, and ripening kinetics, as well as the final NC size at $t = 1200$ s. The high degree of control the nucleation phase exerts over the subsequent growth kinetics is emphasized by the fact that we observe higher ripening rates and slower growth rates in systems with higher initial supersaturations.

Panel D shows the standard deviation as a function of time throughout the reaction. It can be seen that the SD increases rapidly at early times to a maximum. Careful analysis of the data presented in Panels A, C, and D indicate that broadening of the PSD occurs throughout the nucleation phase. This is a consequence of the disparity between the mean radius of the fast growing PSD and the smaller size of the newly formed nuclei (r_{crit}). Following nucleation, the SD then rapidly decreases due to a combination of NC dissolution and the faster growth of the smaller NCs within the evolving PSD. Importantly, simultaneous ripening and sharpening is observed, contrary to the notion that ripening is always accompanied by broadening of the PSD. At longer times all the standard deviations converge to similar values except for the system with $S_{\text{init}} = 8000$, which has a 0.6% lower SD, likely a result of reduced long-term ripening and low growth rates.

Finally, Panel E displays the final PSDs at $t = 1200$ s for the four systems investigated here. All the PSDs are seen to possess a tail extending to smaller NC sizes. The combined data of Panels A–E demonstrate that a strategy to achieve smaller NC sizes is to increase the initial monomer concentration to ensure high nucleation rates. Using the simulated conditions outlined here, reasonable distributions of NCs with appreciable concentrations in the size range 3.5–4 nm have been achieved. The small resulting size range suggests that altering γ (and ξ), through the use of appropriate ligands, is a necessary modification to the reaction conditions in order to obtain NCs with sizes tunable over a wider range.

Effect of Injection Temperature. In this section the effect of injection temperature, T_{inj} , on nucleation and growth is explored. In order to optimize the batch synthesis of NCs it is common to alter the initial reaction temperature such that a favorable balance between the kinetics and thermodynamics of nucleation and growth is achieved. High initial temperatures ensure high collision rates and successful reaction between the precursor molecules, while lower growth temperatures reduce the solubility of the resultant nanocrystals and thereby minimizes ripening. This methodology is referred to as the “hot injection” method. For the simulations outlined here the injection temperatures were set between 553 and 593 K as typical synthetic methods used for the production of NCs are accomplished using these initial temperatures.^{3,29,38,39} The growth temperature in all systems was set at 503 K. $[C]_{\infty}$ was set at 0.004 mol m⁻³ and S at 10 664.

Figure 10 Panel A shows a plot of the simulated reaction temperatures as a function of time for $T_{\text{inj}} = 553$ (dashed line), 573 (solid line), and 593 K (dot-dash line). The reaction temperatures in all systems are seen to converge at the growth temperature at around 600 s. The open circles are digitally recorded reaction temperatures obtained from a typical “hot injection” synthesis. Figure 10 Panel B displays R_{nuc} as a function of time. Upon increasing the injection temperature from 553 to 593 K the initial nucleation rate ($t = 1$ s) is seen to increase by around an order of magnitude from ~ 0.7 to ~ 10 $\mu\text{M s}^{-1}$. As the reaction progresses R_{nuc} is observed to decrease faster in systems with higher initial temperatures. At ~ 15 s the nucleation rates converge to similar values. For reaction times longer than ~ 15 s higher values of R_{nuc} are observed in systems with lower temperatures. The crossover at 15 s (see circle in Panel B) indicates a switch in nucleation kinetics from temperature dominated nucleation rates to nucleation rates that are governed largely by the number of monomers remaining in solution. Specifically, the system with $T_{\text{inj}} = 553$ K has 90% unreacted monomer in solution at $t = 15$ s compared to 49% for the reaction conducted with $T_{\text{inj}} = 593$ K. As a direct consequence nucleation continues for around 60 s in the system with $T_{\text{inj}} = 553$ K and only 35 s for nucleation at 593 K. Comparison of the data in Panels B and D reveal a direct link between the initial rates and duration of nucleation and the SD of the PSDs. In each individual system the SD is seen to reach a maximum close to the end of nucleation, which is higher for systems evolving at lower temperatures. The fact that nucleation lasts around twice as long upon decreasing the injection temperature from 593 to 553 K (coupled with faster initial growth rates) culminates in a SDs 4–5% greater at the end of nucleation.

Panel C shows the concentration of NCs as a function of time throughout the reaction. As observed in Figure 9 we see that the concentration of NCs reaches a maximum and then declines more rapidly in systems that have nucleated more NCs. Examination of the early times in Panels D and E reveals that narrowing of the PSD following nucleation occurs only during the fast growth of the NCs. Once the growth rate falls below some critical value narrowing of the PSD no longer occurs. At longer times, NC growth slows down and a slow broadening of the PSD is observed.

Collectively, the data of Figure 10 shows that lower injection temperatures result in poorer nucleation, as evidenced by reduced concentrations of nanocrystals and broader distributions at the end of the nucleation phase. It is clear that varying the injection temperature allows tunability of the final NC size, with $T_{\text{inj}} = 553$ K resulting in 5 nm NCs after 20 min of growth compared to 3.2 nm NCs for $T_{\text{inj}} = 593$ K. The final PSDs are plotted in Panel F for reference. Unfortunately, there exists an apparent trade off between NC size and concentration. To achieve high yields of larger NCs, it is therefore necessary to employ high temperatures of injection in order to nucleate large numbers of particles and then supplement the reaction with additional monomer, which will allay ripening and promote extended growth and narrowing of the PSD.

Modeling CdSe Nucleation and Growth. To effectively model NC nucleation and growth, the simulation results must be able to simultaneously replicate the concentration and average size of the pariticles. Furthermore, the PSDs obtained at the end of the simulation must agree well with the experimental distributions as determined from HRTEM analysis. In this section we model the nucleation and growth of CdSe NCs. To accomplish these simulations the following parameters were

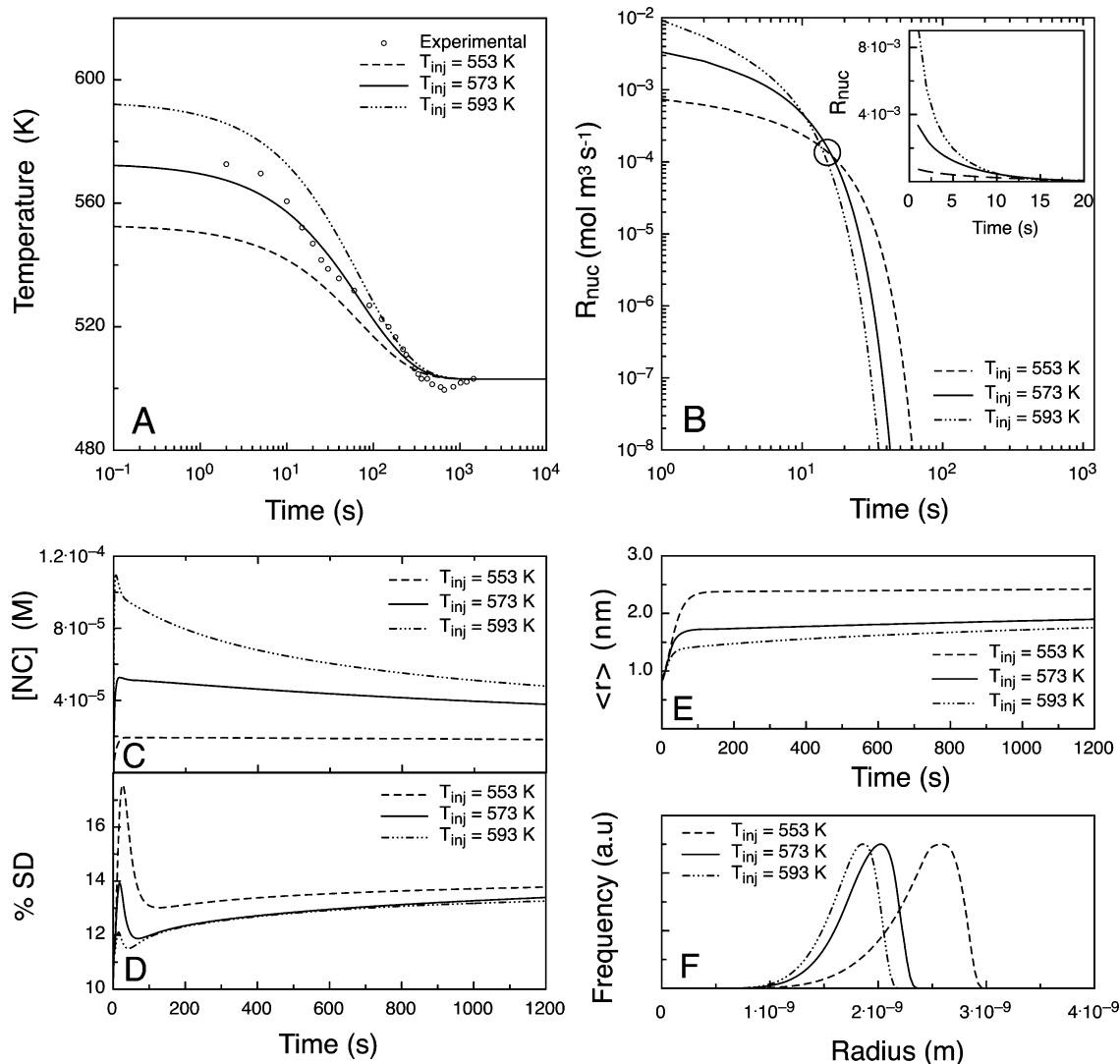


Figure 10. (A) Temperature, (B) R_{nuc} , (C) [NC], (D) SD, and (E) mean radius, \hat{r} as a function of time. (F) Plot of the scaled PSDs at the termination of the reaction.

employed, $V_m = 1.645 \times 10^{-5} \text{ m}^3 \text{ mol}^{-1}$, $r_m = 1.868 \times 10^{-10} \text{ m}$, $\rho = 5.816 \times 10^6 \text{ g m}^3$, $M_W = 95.68 \text{ g mol}^{-1}$, $D = 1 \times 10^{-10} \text{ m}^2 \text{ s}^{-1}$, and $[C]_\infty = 1 \times 10^{-2} \text{ mol m}^{-3}$, as appropriate to bulk CdSe-based monomers and NC synthesis in general. Also, $u = 0.48$ and S was set at 3975 with the temperature profile given by $T_{inj} = 573 \text{ K}$ (see previous section), as appropriate to the experimental conditions outlined elsewhere.³ Specifically, we model the effect of increasing concentrations of a typical cationic ligand (oleic acid, OA) on the evolution of CdSe nanocrystals. The experimental data modeled in this section is outlined elsewhere.³ Consistent with changing the concentration of additives in the growth medium, γ and ξ were assigned values to best fit the data. The errors assigned to the particle radius and concentration are $\pm 0.17 \text{ nm}$ and 10%, respectively.⁴⁰

Figure 11 Panels A and B show the diameter and concentration of NCs over time, respectively, for reactions employing different concentrations of OA. We see that the simulations fit the data very well throughout the course of the reaction. However, we note small deviations from the experimental data for $t \lesssim 200 \text{ s}$. As stated earlier, the success of a given simulation also hinges upon the ability of the model to accurately describe the final particle size distribution. Panels C–E display the experimental and simulated final PSDs at 3600 s. For all three cases we see excellent agreement between the predicted and observed distributions.

Consistent with the experimental data presented in Figure 11 and previous experimental reports^{33,37} OA is known to inhibit nucleation and promote growth. Increasing amounts of OA are also known to increase the early time ripening (ETR) of the nanocrystals.³ Given these observations we deduce that OA facilitates the generation of an environment at the NC surface that is more labile with respect to the addition and removal of monomer units. In this case increasing concentrations of OA should culminate in an increase in the surface reaction rate constant k_r . Panel F shows a plot of k_r as a function of [OA], where k_r was determined using eq 14 and the CdSe-specific reaction constants outlined above, as well as the reaction specific values for γ and ξ listed below. We see that increasing [OA] from 180 to 315 mM increases k_r from 1.82×10^{-11} to $4.59 \times 10^{-11} \text{ ms}^{-1} \text{ K}^{-1}$. These changes are brought about by both increases in γ (0.925 J m^{-2} ; 180 mM, 1.000 J m^{-2} ; 225 mM and 1.100 J m^{-2} ; 315 mM) and decreases in ξ (1.5×10^6 , 1.0×10^6 , 5.0×10^5). Although we expect that changes to k_r will plateau in the extremes of both high and low [OA], over the concentration range investigated here, changes to k_r are approximately linear with $dk_r/d[\text{OA}] = 2.1 \times 10^{-13} \text{ m s}^{-1} \text{ K}^{-1} \text{ M}^{-1}$. It is important to note here that as the diffusion constant is only approximately known the value of $dk_r/d[\text{OA}]$ is only semiquantitative.

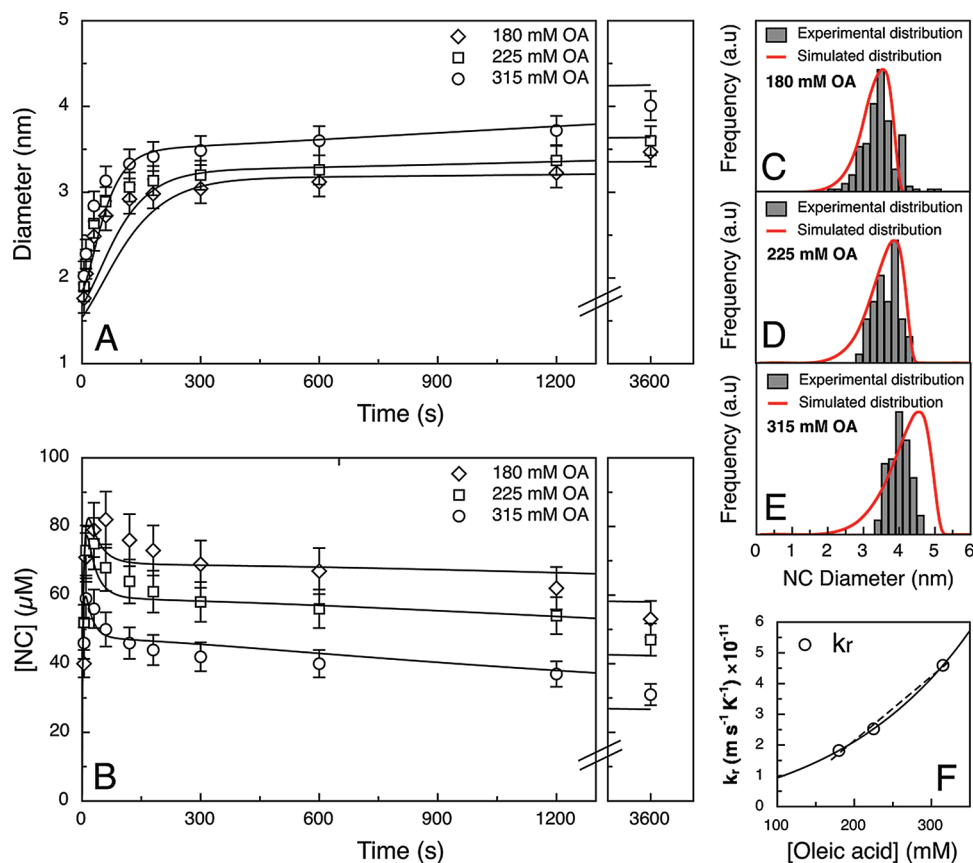


Figure 11. (A) Nanocrystal diameter, (B) nanocrystal concentration, (C) experimental and simulated particle distributions at $t = 3600$ s for reactions containing 180, (D) 225, and (E) 315 mM OA. (F) Plot of the surface reaction rate constant k_r as a function of OA concentration.

The ability to approximate $dk_r/d[L]$ for a range of different ligands (L) and over extended concentration ranges would further aid the predictive powers of the model, the ultimate aim being to apply these numbers in order to predict the outcome of a given reaction scheme. The development of such a strategy would not only deepen our understanding of NC synthesis but also aid in the streamlining of otherwise time-consuming fully empirical approaches to optimizing NC batches.

Concluding Remarks

We have developed a robust numerical scheme to accurately solve the dynamic rate expressions relevant to simultaneous nucleation and growth. It has been shown that, in addition to higher-order upwinding, flux limiters are a necessary inclusion in order to avoid both numerical diffusion and the generation of nonphysical oscillations in the data sets.

The evolution of a distribution of nanocrystals is distinct from the evolution of larger micrometer-size species, as the final crystal sizes are not much larger than the primary nuclei. As a consequence, the final outcome of a nanocrystal synthesis, i.e., mean crystal size, concentration, and standard deviation, is almost solely determined by the end of nucleation. From the simulations performed on NC nucleation and growth, it may be concluded that the evolution of NC in the liquid phase must proceed via highly reaction-limited kinetics. This finding is consistent with experimental results on NC synthesis, which show nucleation and growth to be extremely sensitive to the nature and concentration of the adsorbates in solution.

The simulations performed here successfully replicate the three main aspects of NC evolution observed experimentally, namely: fast growth of the ensemble followed by a quasi-

equilibrium phase that exists prior to the classical Ostwald ripening of the ensemble.

The model implemented here also replicates the strong overlap between nucleation, growth, and coarsening evident in NC syntheses at early reaction times. Furthermore, the simulations employ realistic reaction parameters and have been conducted over time-scales directly applicable to experimentally observed results on NC evolution.

The inclusion of a more detailed particle aggregation mechanism as well as a time and temperature dependent rate expression for the conversion of precursor to monomer constitute further improvements to the current model. Additionally, particle–particle interactions operating through a mean diffusion field may also be included. However, it is expected that interactions of this type would not significantly alter the growth of the NCs, given that under reaction-limited conditions the interfacial concentrations of the particles are quite similar.

Appendix

List of Symbols

- C = Monomer
- C_n = Cluster with n units
- C_∞ = Infinitely large particle (flat surface)
- $[C]_e$ = Concentration of monomer in equilibrium with a particle of radius r
- $[C]_i$ = Concentration of monomer at the particle interface
- $[C]_b$ = Concentration of monomer in the bulk of solution
- $[C]_\infty$ = Concentration of monomer in equilibrium with an infinitely flat surface
- D = Diffusion coefficient

I_{react} = Total reaction driven flux

I_{diff} = Total diffusion driven flux

I^{SS} = Total steady state flux

J = Molar flux

k_{r} = Monomer surface reaction rate constant

k_{des} = Monomer desorption rate constant

k_{obs} = Observed reaction rate constant

$k_{1,p}$ = Collision frequency between monomer and a critical cluster

$k_{1,n}$ = Forward reaction rate between monomer cluster of n units

$k_{-1,n}$ = Backward reaction rate between monomer cluster of n units

$K_{1,n}$ = Equilibrium constant for the reaction $C + C_n \rightarrow C_{n+1}$

$K_{1,\infty}$ = Equilibrium constant for the condensation of C onto C_{∞}

γ = Surface energy

Γ = Instantaneous growth rate

$\Gamma_{i+1/2}$ = Advective velocity at the east boundary of i

$\Gamma_{i-1/2}$ = Advective velocity at the west boundary of i

$g(r)$ = Nuclei distribution function

$\Delta G_{1,n}^0$ = Total free energy change at standard states for $C + C_n \rightarrow C_{n+1}$

$\Delta G_{1,\infty}^0$ = Total free energy change at standard states for the condensation of C onto C_{∞}

$\Delta G_{1,n}^{\text{vol}}$ = Volume free energy change for $C + C_n \rightarrow C_{n+1}$

$\Delta G_{1,n}^{\text{surf}}$ = Surface free energy change for $C + C_n \rightarrow C_{n+1}$

ΔG_v = Volume-normalized free energy

M_w = Molecular weight

N_i = Frequency in the i th population

N_A = Avogadro constant

p = Number of units in a cluster of critical size

Ψ = Flux limiter function

r_{crit} = Critical radius

r_m = Radius of monomeric unit

r = Particle radius

\hat{r} = Mean radius of the distribution

ρ = Macroscopic density

R = Universal gas constant

σ = Distance from the center of a particle to $[C]_b$

S^t = Supersaturation at time t

$S^{t+\Delta t}$ = Supersaturation at time $t + \Delta t$

T = Temperature

u = Coagulation coefficient

V_m = Molar volume

V_{tot} = Simulated reaction volume

Δ^+ and ∇^- = Gradient operators

Acknowledgment. J.v.E. acknowledges support through an APA scholarship. P.M. thanks the ARC and the University of Melbourne for support through the Federation Fellowship program.

Supporting Information Available: Plots of the nucleation and growth rates for various initial parameters. Various MUSCL

Flux limiter test simulations. Schematic of code. This material is available free of charge via the Internet at <http://pubs.acs.org>.

References and Notes

- (1) Chen, Y.; Johnson, E.; Peng, X. *J. Am. Chem. Soc.* **2007**, *129*, 10937–10947.
- (2) Wong, E. M.; Bonevich, J. E.; Searson, P. C. *J. Phys. Chem. B* **1998**, *102*, 7770.
- (3) van Embden, J. L.; Mulvaney, P. *Langmuir* **2005**, *21*, 10226–10233.
- (4) Qu, L.; Yu, W. W.; Peng, X. *Nano Lett.* **2004**, *4*, 465–469.
- (5) Shevchenko, E. V.; Talapin, D. V.; Schnablegger, H.; Kornowski, A.; Festin, O.; Svedlindh, P.; Haase, M.; Weller, H. *J. Am. Chem. Soc.* **2003**, *125*, 9090–9101.
- (6) Sugimoto, T.; Chen, S.; Muramatsu, A. *Colloids Surf., A* **1998**, *135*, 207–226.
- (7) Henglein, A. *Chem. Rev.* **1989**, *89*, 1861–1873.
- (8) Kahlweit, M. *Adv. Colloid Interface Sci.* **1975**, *5*, 1–35.
- (9) Langer, J.; Schwartz, A. *Phys. Rev. A* **1979**, *21*, 948–958.
- (10) Lifshitz, I. M.; Slyozov, V. V. *J. Phys. Chem. Solids* **1961**, *19*, 35.
- (11) Wagner, P. E.; Franz, G. P. *J. Colloid Interface Sci.* **1975**, *53*, 429–438.
- (12) Sugimoto, T. *Adv. Colloid Interface Sci.* **1987**, *28*, 65–108.
- (13) Robson, J. *Acta Mater.* **2004**, *52*, 4669–4676.
- (14) Robson, J. *Mater. Sci. Technol.* **2004**, *20*, 441–448.
- (15) Myhr, O.; Grong, O. *Acta Mater.* **2000**, *48*, 1605–1615.
- (16) Madras, G.; McCoy, B. J. *Chem. Eng. Sci.* **2003**, *58*, 2903–2909.
- (17) Yao, J.; Elder, K.; Hong, G.; Grant, M. *Phys. Rev. B* **1991**, *45*, 8173–8176.
- (18) Kumar, S.; Ramkrishna, D. *Chem. Eng. Sci.* **1996**, *51*, 1311–1332.
- (19) Alexopoulos, A.; Roussos, A.; Kiparissides, C. *Chem. Eng. Sci.* **2004**, *59*, 5751–5769.
- (20) Boris, J.; Book, D. J. *Comput. Phys.* **1973**, *38*, 69.
- (21) Zalesak, S. J. *Comput. Phys.* **1979**, *31*, 335–362.
- (22) Talapin, D. V.; Rogach, A. L.; Haase, M.; Weller, H. *J. Phys. Chem. B* **2001**, *105*, 12278–12285.
- (23) Thessing, J.; Jianghong, Q.; Haiyan, C.; Pradhan, N.; Peng, X. *J. Am. Chem. Soc.* **2007**, *129*, 2736–2737.
- (24) Robb, D.; Privman, V. *Langmuir* **2007**, *24*, 26–35.
- (25) Mantzaris, N. *Chem. Eng. Sci.* **2005**, *60*, 4749–4770.
- (26) Kwon, S.; Piao, Y.; Park, J.; Angappane, Y.; Hwang, N.; Park, J.-G.; Hyeon, T. *J. Am. Chem. Soc.* **2007**, *129*, 12571–12584.
- (27) Riberio, C.; Lee, E.; Longo, E.; Leite, E. *ChemPhysChem* **2005**, *6*, 690–696.
- (28) Soon, G.; Piao, Y.; Park, J.; Angappane, S.; Jo, Y.; Hwang, N.; Park, J.; Hyeon, T. *J. Am. Chem. Soc.* **2007**, *129*, 12571–12584.
- (29) Peng, X.; Wickham, J.; Alivisatos, A. P. *J. Am. Chem. Soc.* **1998**, *120*, 5343–5344.
- (30) van Leer, B. *J. Comput. Phys.* **1979**, *32*, 101–136.
- (31) Hirsch, C. *Numerical Computation of Internal and External Flows*; John Wiley and Sons: New York, 2000; Vol. 2.
- (32) Press, W.; Flannery, B.; Teukolsky, S.; Vetterling, W. *Numerical Recipes: The Art of Scientific Computing*; Cambridge University Press: New York, 1986.
- (33) Yu, W. W.; Peng, X. *Angew. Chem., Int. Ed.* **2002**, *41*, 2368–2371.
- (34) Li, L. S.; Pradhan, N.; Wang, Y.; Peng, X. *Nano Lett.* **2004**, *4*, 2261–2264.
- (35) Atkins, P. W. *Physical Chemistry*, 5th ed.; Oxford University Press: Oxford, 1994.
- (36) Wagner, C. Z. *Elektrochem.* **1961**, *65*, 581.
- (37) Bullen, C. R.; Mulvaney, P. *Nano Lett.* **2004**, *4*, 2303–2307.
- (38) Jasieniak, J.; Bullen, C.; van Embden, J. L.; Mulvaney, P. *J. Phys. Chem. B* **2005**, *109*, 20665–20668.
- (39) Murray, C. B.; Norris, D. J.; Bawendi, M. G. *J. Am. Chem. Soc.* **1993**, *115*, 8706–8715, got 175.
- (40) Yu, W. W.; Qu, L.; Guo, W.; Peng, X. *Chem. Mater.* **2003**, *15*, 2854–2860.

JP9027673